RTO AVT Symposium on ADVANCED FLOW MANAGEMENT

PART A – VORTEX FLOW AND HIGH ANGLE OF ATTACK

Paper Number 44

Cranked Arrow Wing (F-16XL-1) Flight Flow Physics with CFD Predictions at Subsonic and Transonic Speeds

John E. Lamar
NASA Langley Research Center, M.S. 499
Hampton, Virginia 23681-2199 USA

Cranked Arrow Wing (F-16XL-1) Flight Flow Physics with CFD Predictions at Subsonic and Transonic Speeds

John E. Lamar
NASA Langley Research Center, M.S. 499
Hampton, Virginia 23681-2199 USA

Summary

The CFD modeling used has produced reasonably good global upper-surface pressure coefficient comparisons with measured flight data at both transonic and subsonic speeds at the angles of attack presented. Boundary layer comparisons showed the profiles to be reasonably well predicted inboard and under the primary vortex system. However, the secondary vortex profile was not well predicted either at the anticipated separation point or under the secondary vortex. Moreover, the flight data showed there to be a vortex/boundary-layer interaction that occurred in the vicinity of the secondary vortex. The spanwise distribution of local skin friction measured data was reasonably well predicted, especially away from the wing leading-edge. Lastly, predicted and measured flight-pressures, as well as flight-image data, for the F-16XL-1 airplane are now available via the World Wide Web.

Introduction

The increasing capability of CFD to simulate real airplane geometries and flow conditions is found in the literature for both fighter and transport airplanes, for example, the F-18 HARV (ref. 1) and the MD-11 (ref. 2). In the continuance of that trend, this report details the results of a comparative study of CFD and flight data for the F-16XL-1 airplane (fig. 1) over a wide range of test conditions from transonic to subsonic speeds. Though this airplane is not new, its cranked-arrow planform is relevant to any high-speed (supersonic) fighter or transport configuration.

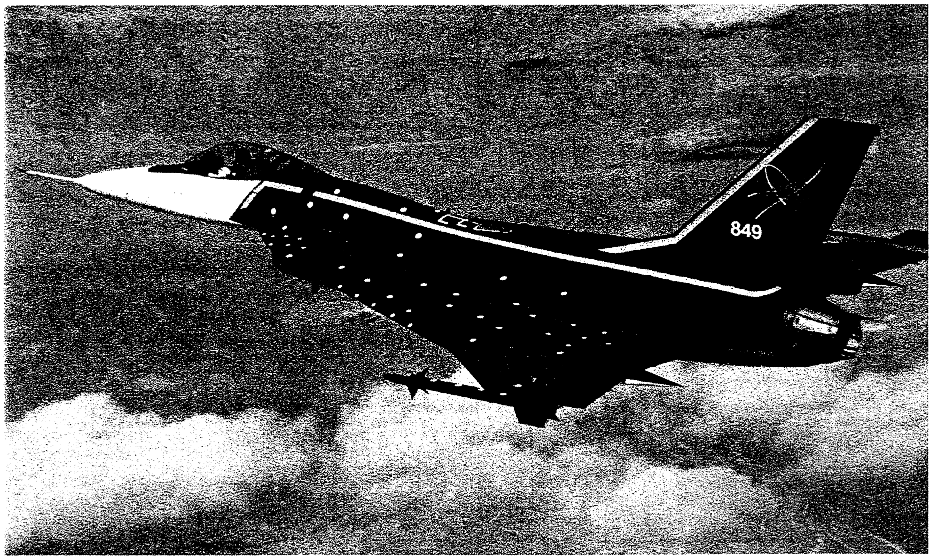

Figure 1. F-16XL-1 airplane in flight with missiles, tufts, modified flow-visualization paint-scheme and video targets at NASA-Dryden.

When the F-16XL-1 airplane was new, the kinds of testing done were related to its operational characteristics (refs. 3 and 4) and not focused on an understanding of its basic flow physics, the subject of the current investigation. (This airplane is not to be confused with the two-seat version – the F-16XL-2 airplane – detailed in reference 5 and which was used to examine the boundary layer flow for the Supersonic Laminar Flow Control flight experiments; work done in support of the High Speed Research program.) The flow physics understanding sought for the F-16XL-1 airplane was the subject of the Cranked-Arrow Wing Aerodynamics Project (CAWAP), as reported in reference 6, and consisted primarily of surface features, such as pressures, local flow, boundary-layers, and skin friction. Selected comparisons of predicted and measured quantities at $1g$ –flight from reference 6 form the scope of this paper. Geometrical consistency between the full-airplane, including wing-tip mounted missiles and tail, and the CFD model was also an important issue for the CAWAP. Reference 6 notes that reasonably good overall agreement was achieved – the agreement very good over much of the wing – between the upper-surface outer-mold-line and the numerical-surface-description of the airplane with the flaps undeflected. Hence, the expectation is that the predicted results will adequately represent the flow physics measured on the airplane.

Extensive use of the World Wide Web was made to generate the comparisons presented herein.

Symbols and Abbreviations

BL	butt line on airplane, in., positive on right wing (see fig. 2)
CFD	Computational Fluid Dynamics
CAWAP	Cranked-Arrow Wing Aerodynamics Project
C_p	static-pressure coefficient
c_f	local skin friction coefficient
EFD	Experimental Fluid Dynamics, flight- or ground-based measurements
ESP	Electronic Scanning Pressure
FAST	Flow Analysis Software Toolkit
FC	Flight Condition (see ref. 6)
FS	fuselage station on airplane, in., positive aft (see fig. 2)
g	acceleration due to gravity; 32.2 ft/sec^2
HUD	heads-up display
h	airplane altitude, ft
I.D.	inside diameter
i,j,k	grid indices
LE	leading edge
M_∞	free-stream Mach number
O.D.	outside diameter
R_n	Reynolds number
r	vortex core radius
T	absolute temperature, °R
V/V_{RE}	ratio of velocity magnitude in boundary layer to that at the Rake Extreme total-pressure tube
WL	waterline on airplane, in., positive up (see fig. 2)
x/c	fractional distance along the local chord, positive aft
y	normal distance above the surface at a rake location, in.
y^+	R_n like term for flat-plate turbulent boundary layer
α	angle of attack, deg
β	angle of side-slip, deg

Subscripts

avg	average value
nom	nominal value
u	upper surface

F-16XL-1 Airplane and CFD Modeling

General arrangement

The F-16XL-1 airplane is a single-place fighter-type prototype airplane developed by the General Dynamics Corporation-Ft.Worth Division (now the Lockheed Martin Tactical Aircraft Systems) by stretching the fuselage of a Full-Scale Development F-16A and adding a cranked-arrow wing, a modified fuel system, and a modified flight control system. This airplane had scheduled leading-edge flaps, elevons, and ailerons on the wing for control. The technical specifications for the airplane are given in Table 1. Details on the construction of the airplane and its intended missions are given in references 3, 4, and 7.

Table 1. – Airplane Specifications

Feature	Value
Wing Span	32.4 ft.
Height	17.606 ft.
Length	54.155 ft.
Reference Chord	24.7 ft.
Theoretical Root Chord	41.75 ft.
Wing Area	646.37 ft^2
Reference Wing Area	600 ft^2
Reference Aspect Ratio	1.75
Typical Takeoff Weight	35,000 lbs.
Engine; Max Thrust	Pratt & Whitney F100-PW-200; 23,830 lbs.

The design of the cranked-arrow wing was a cooperative effort of the NASA Langley Research Center and the General Dynamics Corporation. The new wing was designed to provide the F-16

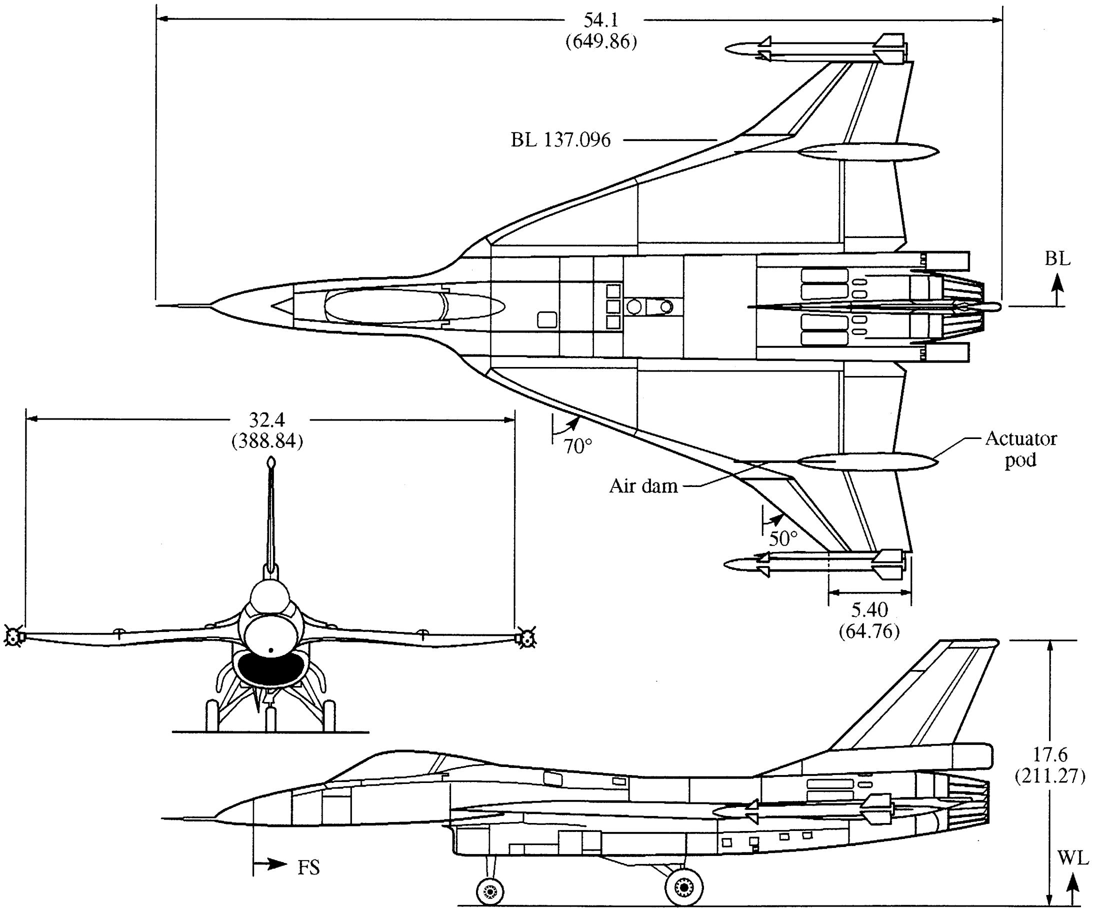

Figure 2. Three-view drawing of the F-16XL-1 airplane.

airplane with improved supersonic performance while maintaining transonic performance comparable with that provided by the current F-16 design. As shown in figure 2, the resultant design had a leading-edge sweep angle of 70° inboard and 50° outboard of the crank. At the juncture of the wing leading edge with the fuselage, an "S-blend curve" was placed in the leading edge to alleviate a pitch instability that occurred at high angles of attack in wind-tunnel tests. Because the wing sweep and general arrangement of the cranked-arrow wing of the F-16XL-1 are still representative of high-speed configurations, this airplane was selected for study. All flight tests reported herein were with the air dams – upper-surface fences mounted near the wing leading-edge crank – and wing-tip missiles installed, as shown in figures 1 and 2.

Instrumentation suite

Seven different kinds of flight data were collected; four are shown schematically in figure 3. Three were pressure based – surface static pressures, boundary-layer rakes, and modified Preston tubes (ref. 8); three were video-recording based – surface tufts, surface oil and surface liquid crystals; and one was hot-film data. The pressure and surface-flow-data are used for the purpose of establishing the effects of variation in Mach number on the local flow. These data serve as the basis for comparison with other data sets. The hot-film data are used to establish whether boundary-layer transition occurs and under what test conditions. (See reference 6 for a complete set of comparisons.)

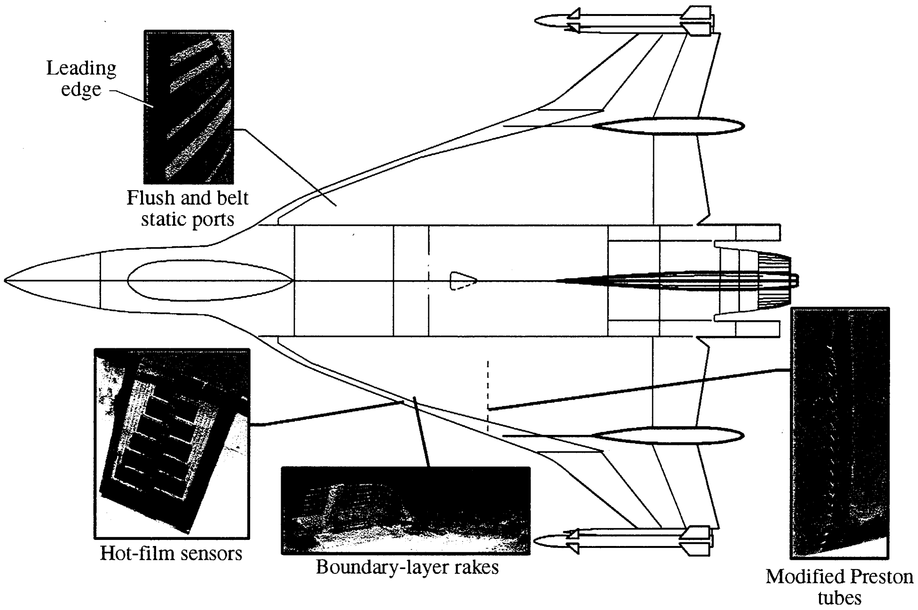

Figure 3. Schematic of airplane instrumentation suites on the surface of the airplane.

Pressure suites

Figures 4 and 5 detail the complete pressure instrumentation system layout on the airplane, including the distribution of the static ports by type, belt or flush, and boundary-layer rakes or modified Preston tubes. These static ports are connected to internally mounted Electronically Scanning Pressure (ESP) transducers – also called modules – through 0.0625 inch O.D. tubes (0.028 inch I.D.). Each pressure-tube in the belt was used to measure two separate values of pressure. This measurement was accomplished by sealing each tube about halfway along its length, thereby provision was made for one forward and one aft port. The numbers associated with the belt static ports in figure 4 were the values of the actual ports for that belt.

The right-wing surface pressures – mostly upper surface – were measured using 337 static ports, both flush and in streamwise belts, through eleven 32-port ESP modules. (For the leading-edge ports 10 psi modules were used and 5 psi modules elsewhere.) Of these 337 ports, only 326 proved to be reliable and the distribution was 280 on the upper surface and 46 on the lower. The ports were arranged so that there would be a sufficient number at a given BL or FS for cross plotting, as well as for covering other regions of special interest; i.e., the apex ahead of/and

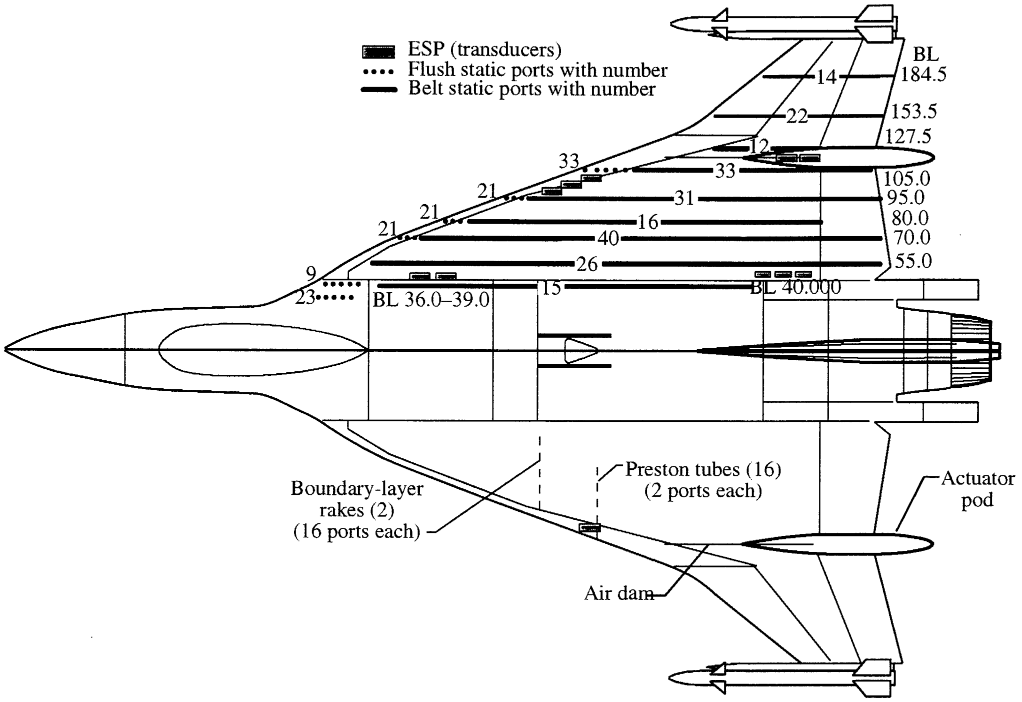

Figure 4. Details of complete-pressure-instrumentation suite and layout on the airplane.

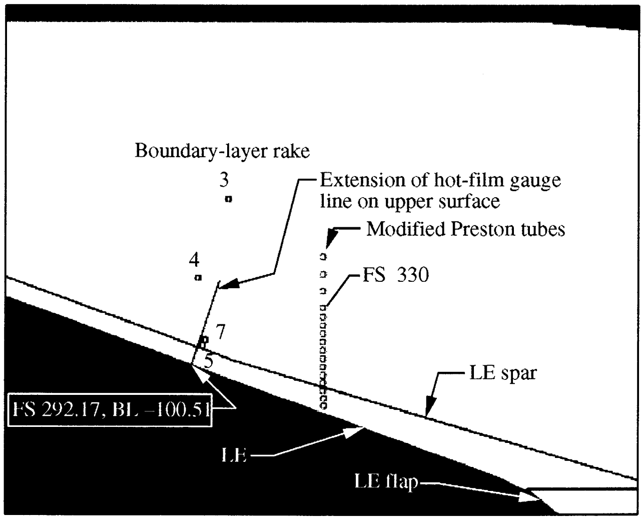

Figure 5. General arrangement of rake and modified Preston tube locations on F-16XL-1 left wing; pressure instruments oriented for α=13°; M_∞=0.29; and R_n=46.1x10^6.

behind the hinge-lines of the trailing-edge control-surfaces.

Boundary-layer (B.L.) measurements were made by using two rakes at a time at four different positions on the left wing with the most inboard one always used as a control. Each rake used 16 active tubes, 15 total pressure and 1 static pressure, of the 23 available. These two rakes were connected to one 32-port ESP module located inside the left wing When mounted on the airplane, each rake was oriented into the local flow at an average angle over its height based on initial CFD predictions from the CFL3D code (refs. 9 and 10). The flow conditions were for the complete airplane (half-airplane modeled with symmetry assumed) $\alpha = 13°$, $M_\infty = 0.29$ and $R_n = 46.1x10^6$; i.e. Flight Condition (FC) #7.

Figure 5 shows the four locations chosen – one well inboard of the shed vortex systems, one underneath the primary vortex, and two associated with the secondary vortex, both underneath and at its separation point; all are at a nominal position of FS~295 along the predicted orientation which takes into account the flow at and slightly off the surface. The average of these local flow directions was used to establish the rake orientation angles. The average of the local flow at- and slightly off-the-surface were used to establish the rake orientation angles for FC#7. This figure also shows the relative locations of the modified Preston tubes. They were to be located at the same fuselage station as the boundary-layer rakes, but a more aft position for the tubes was necessitated due to easier airplane installation and to avoid the flow off a step in the leading-edge region.

The 16 modified Preston tubes (See figs. 3 and 5) – the modification to each Preston tube is the integration of a static pressure port with the total pressure tube – are used for the determination of local skin friction across the left wing near FS 330. These 32 pressures use the same ESP as the rakes but not on the same flight. The tubes were aligned with the local flow by using the same initial CFL3D solution at FC#7. The equation used to generate the EFD c_f values comes from reference 8 and relates, through a process of calibration, the pressure change between the total and static tubes to the local skin friction.

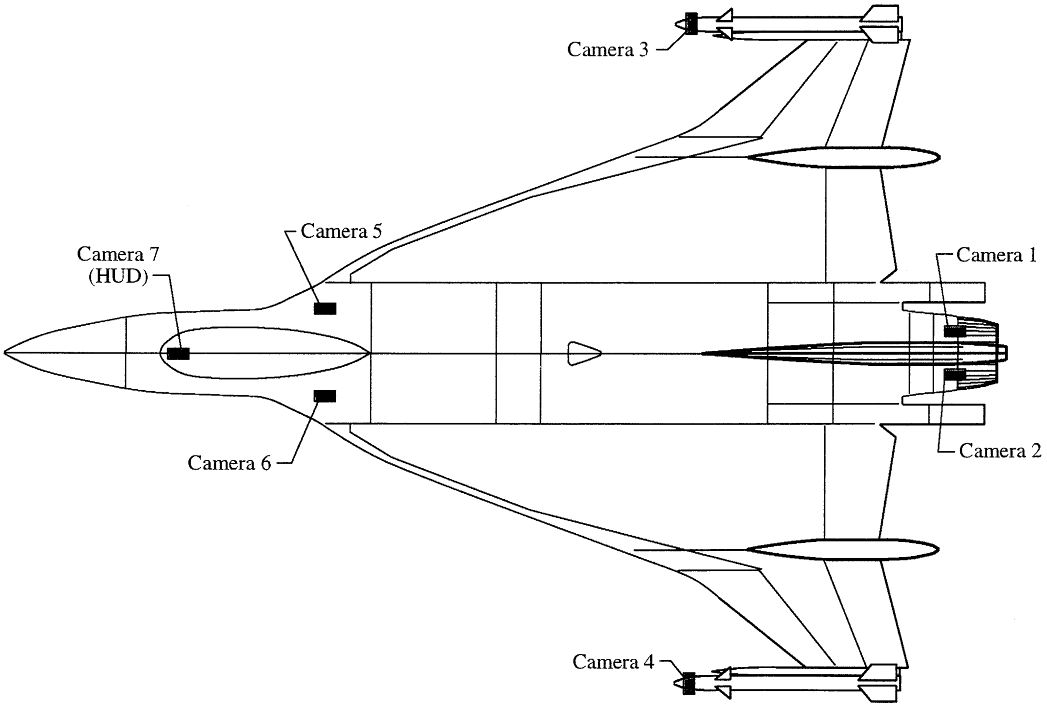

Figure 6. Locations of the video suite on the F-16XL-1 airplane.

Video suite

Video data were recorded with up to six external cameras: two mounted atop the vertical tail, one on either side of the fuselage behind the canopy, and one in the nose of each dummy missile. An internally mounted heads-up display (HUD) camera was also used on occasion. Figure 6 shows the camera locations on the airplane. The time was added to each image by a time-code inserter (See appendix C of ref. 6) so that the images could be compared to form a composite and the flight test conditions could be established. Images of interest were digitized in a 512- by 480-pixel format for further processing to develop quantifiable video data. In addition to the images, the other input quantities needed for the processes are the video targets and the position and calibration characteristics of each camera/lens combination.

CFD modeling

The flow solver code CFL3D was run in the Navier-Stokes mode with a turbulent boundary layer employing the Baldwin-Lomax with the Degani-Schiff turbulence model (in the *j-k* directions) on a multiblock, patched grid over a variety of wind-tunnel and flight test conditions. Two separate grids were used to model half the airplane configuration (with undeflected control surfaces) and external flow field. The initial grid had 36 blocks and was used with version 3 of the flow solver to produce the initial results upon which the locations and orientations of the surface instrumentation were set. The current grid had 30 blocks and was used with version 5 of the flow solver to obtain the comparative solutions reported herein. The current grid was needed for two reasons: (1) to have the grid more closely conform to the actual fuselage and wing geometries and (2) to improve the grid layout on the wing and fuselage surfaces; for either grid the missile- and missile-rail-grids which were effectively unchanged. For the current grid, the inner region of the airplane was modeled by 16 blocks, the outer region by 14 blocks, and all 30 blocks are shown schematically in figure 7. The boundary conditions were symmetry, solid wall for the outer mold lines, flow into the duct inlet with the exhaust face faired over, and Riemann-type conditions at the far-field boundaries. A total of 1,372,096 cells (1,707,117 node points) were used to obtain solutions at specified test conditions (i.e., α, M_∞, grid R_n, T, etc.). To maximize computer resource allotments, the minimum number of cells was used. The resulting grid spacing normal to the numerical surface led to a value of y^+ of 2 at wind-tunnel R_n, whereas at flight R_n the average value was y^+ of 82. In an effort to compensate for the insufficient grid spacing at flight conditions, the "wall function" option was used to augment the turbulence model in CFL3D. The wall function is defined as that boundary-layer growth rate expected from a turbulent mean flow near the wall (ref. 11).

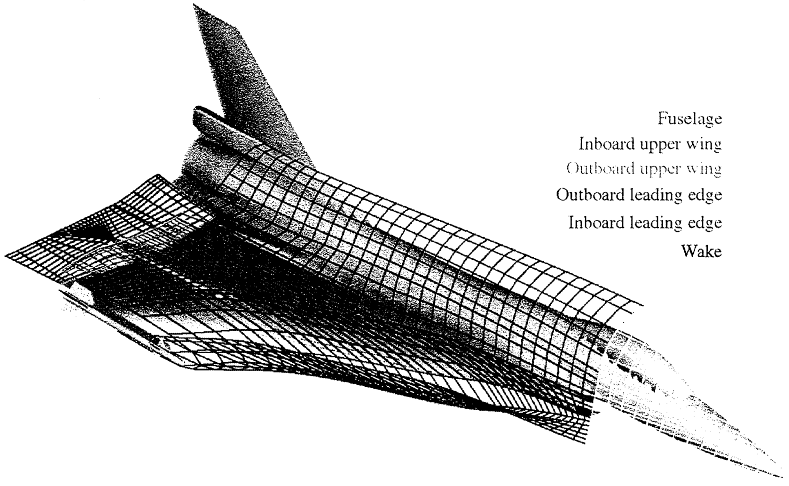

(a) Inner.

Figure 7. CFD block structure layout for F-16XL-1.

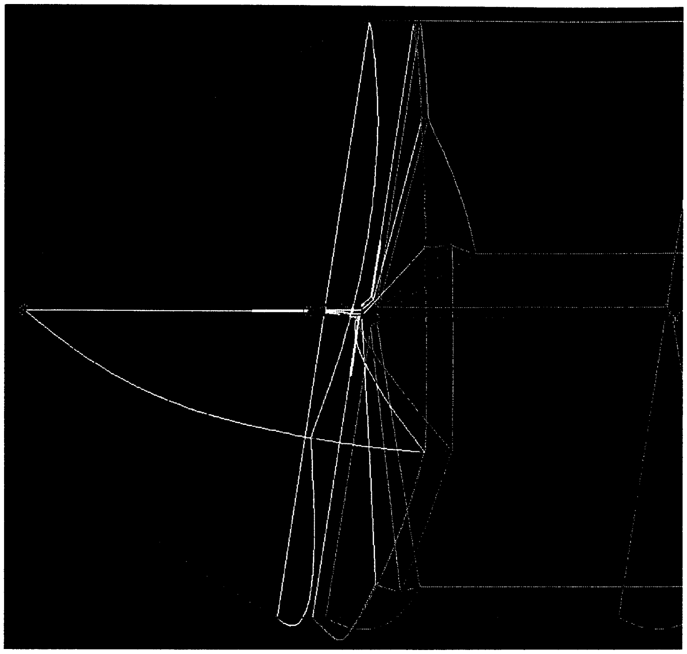

(b) Outer.

Figure 7. Concluded.

Transonic Comparisons

Upper surface pressures

Figure 8 was developed by using FAST (ref. 12) and shows an overall comparison of CFD and flight C_p data at $\alpha = 4.4°$ and $M_\infty = 0.97$ (FC#70 – Flight 152 Run 5B). Here the CFD solution data serve as the background-color mirrored about the centerline and with the flight C_p data superimposed. The flight port locations are denoted as black-dots and the associated C_p values by the color of the surrounding bubble-outline. The comparison, including the insert, indicates there to be very good overall agreement using this global C_p scale in that the colors of the bubble-outlines are virtually indistinguishable from the CFD over the wing. However, chordwise and spanwise comparisons are still needed because the C_p global scale at FC #70 is too large for the entire upper-surface of the airplane to capture the details that exist over just the wing alone. These are provided in reference 6 and summarized as follows: remarkable detail agreement was noted to occur all along the leading edge and not only there but along the chords at BL of 40 and 55. Regarding the interest in whether a shock crosses the hinge line of an aft control surface could be detected in flight and predicted at BL=153.5, a shock is noted to occur near x/c=0.75 in the flight data. This location is aft of the aileron hinge line, and this feature is not captured by the CFD of the configuration with undeflected control surfaces.

Upper surface pressure contours

Figure 9 shows C_p upper-surface contours at the same transonic conditions denoted in figure 8 at both flight and CFD. (CFD contours are generated using FAST (ref. 12) and flight contours from Tecplot (ref. 13).) There are many similarities between these contours; overall, the CFD pressures are more negative, especially near the leading-edge and over the aft part of the wing. Along the inboard edges, aft about one-third of the distance from the S-blend curve, both the flight and CFD data of figure 9 show a shock followed by an expansion, whereas outboard only the flight data show a shock aft centered near the aileron hinge line. This elevon shock in flight has been previously noted, and because it does not show up in the CFD solution is most likely attributable to differences in the control-surface deflections. The CFD modeling is with the control surfaces undeflected, whereas the flight experiment has small, but measurable, trailing-edge deflections.

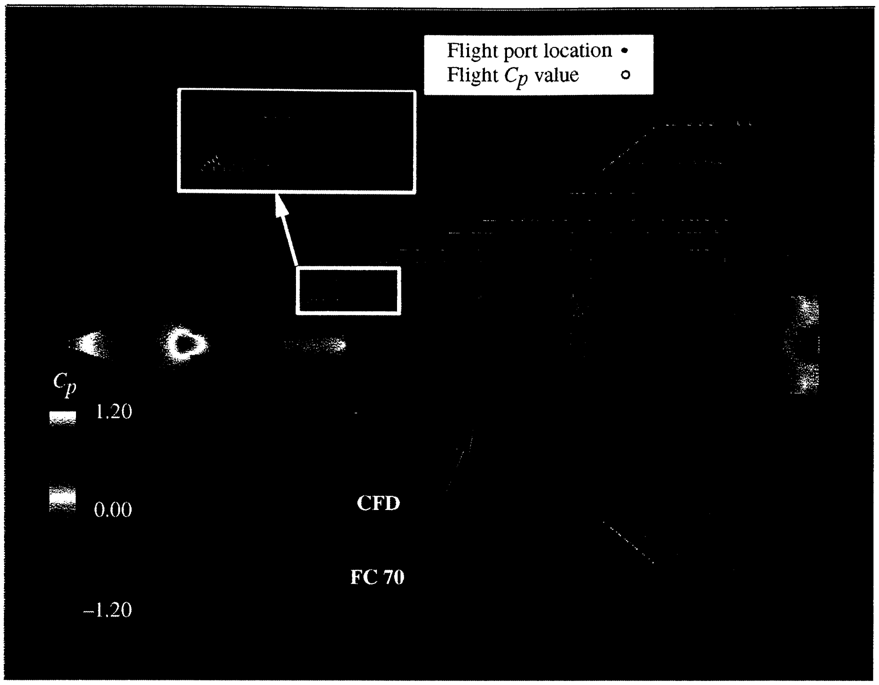

Figure 8. Predicted and measured flight $C_{p,u}$ distribution of F-16XL-1 at FC#70 ($\alpha = 4.4^0$; $M_\infty = 0.97$; $R_n = 88.77 \times 10^6$).

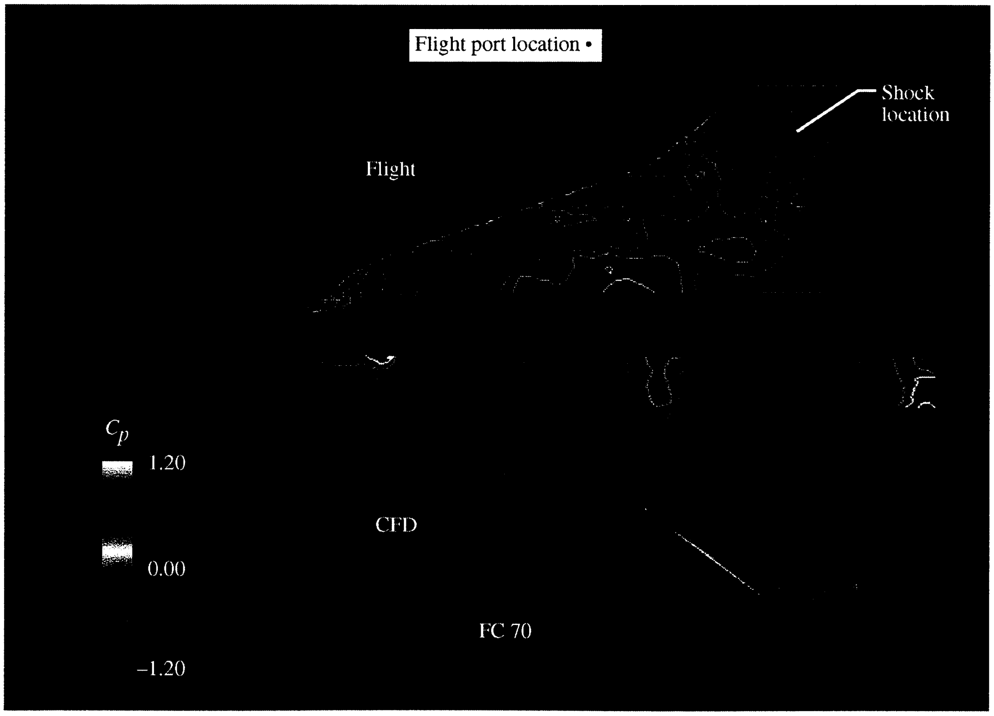

Figure 9. Predicted and measured flight $C_{p,u}$ contours of F-16XL-1 at FC#70 ($\alpha = 4.4^0$; $M_\infty = 0.97$; $R_n = 88.77 \times 10^6$).

Subsonic Comparisons

At α = 5.5°

Upper surface pressures

Figure 10 presents overall comparisons of CFD and flight C_p data for $\alpha = 5.5°$ and $M_\infty = 0.52$ (FC#1 – Flight 152 Run 12B). This figure shows the general overall-agreement to be good in that the colors of the bubble-outlines are indistinguishable from the CFD surface, with its associated C_p color bar, over a large part of the wing. Where differences are noted in this figure, the flight values are seen to be more positive than the CFD values with the exception of six ports in the apex region.

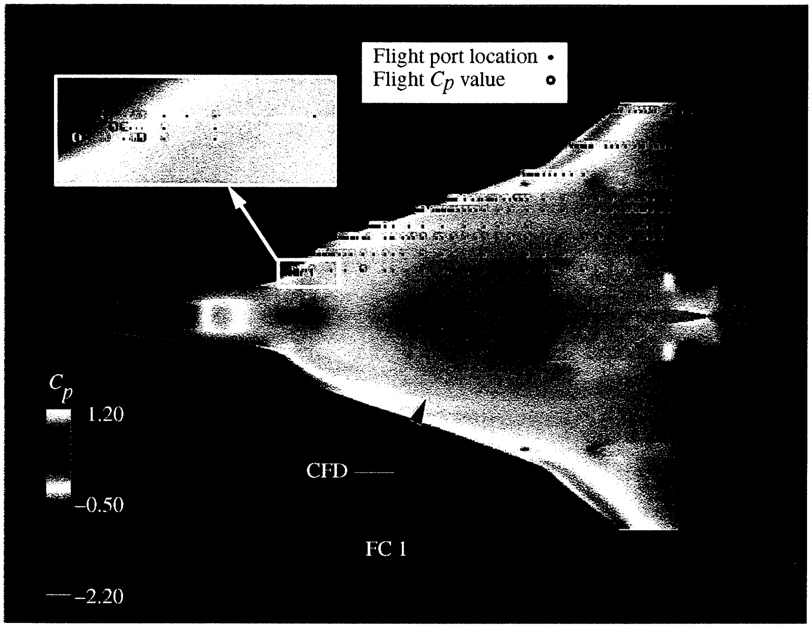

Figure 10. Predicted and measured flight $C_{p,u}$ distribution of F-16XL-1 at FC#1 ($\alpha = 5.5^0$; $M_\infty = 0.52$; $R_n = 77.71 \times 10^6$).

At α = 10.4°

Upper surface pressures

Figure 11 presents overall comparisons of CFD and flight C_p data for $\alpha = 10.4°$ at $M_\infty = 0.53$ (FC#46 – Flight 144 Run 3B) and similar overall agreement is noted to occur at this value of α. Differences noted between the two data sets appear less here due in part to the expanded C_p range. Figure 11 shows some similar patterns to those in figure 10, in that where differences do occur the measured values are generally more positive; however, here they are primarily restricted to the forward part of the wing. The exceptions occur in the apex region where the insert illustrates the measured suction pressures for five ports to be more negative than predicted, that is, a region of strong vortex influence.

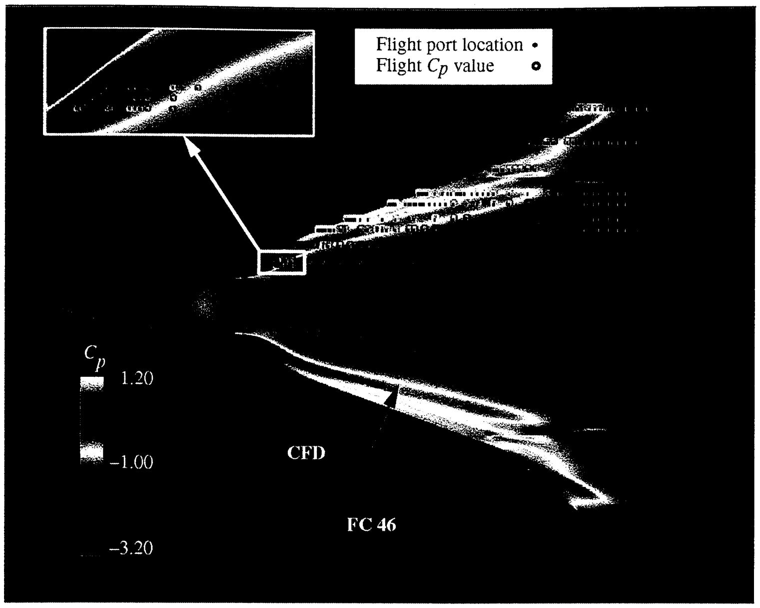

Figure 11. Predicted and measured flight $C_{p,u}$ distribution of F-16XL-1 at FC#46 ($\alpha = 10.40^0$; $M_\infty = 0.53$; $R_n = 46.90 \times 10^6$).

Surface streamlines and vortices with flight tufts

Figure 12 was constructed using FIELDVIEW software (ref. 14) and shows the fusion (overlaying) of surface tuft images from three flight-cameras with CFD surface streamlines and vortex-core representation at $\alpha = 10.4°$ and $M_\infty = 0.53$ (FC#46). In particular, figure 12(a) presents the combination of the three flight-camera images projected onto a grid representation of the airplane. Figure 12(b) shows the CFD surface streamlines to compare well with these tuft images. Figure 12(c) presents iso-surfaces of the stagnation pressure (PLOT3D (ref. 15)) at a value of 0.78 and represents the locations and extent of the various airplane vortex systems. Figures 12(b) and (c), with transparency employed for the vortex systems iso-surfaces, are combined to form figure 12(d). As expected from the results of the surface comparison, the vortex system is well located with respect to the flight tufts.

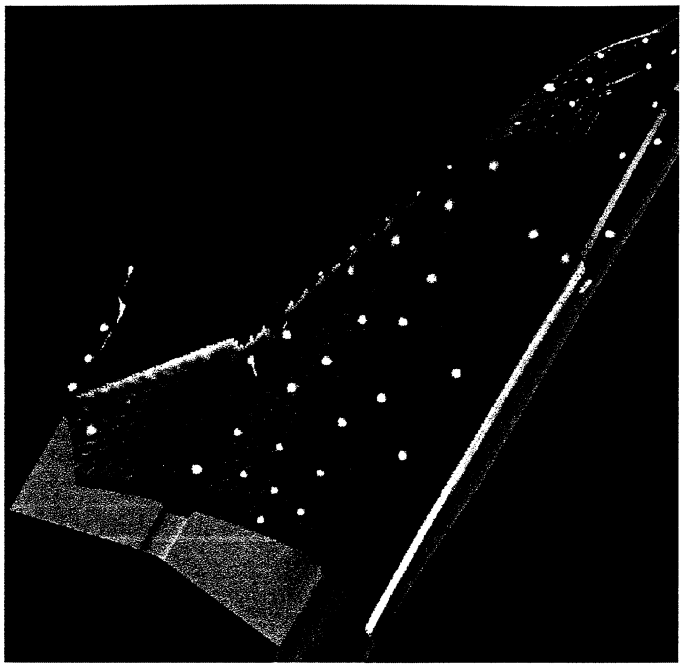

(a) Tuft-images projected from three-cameras on to airplane grid.

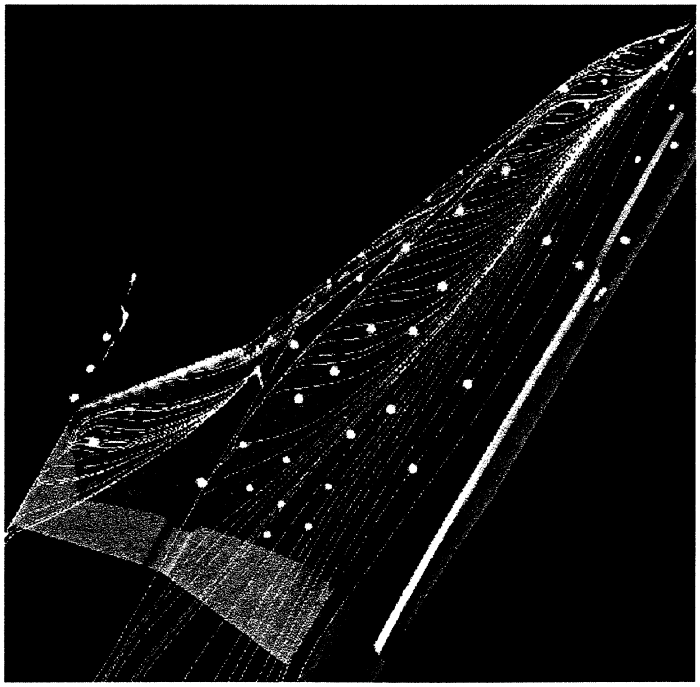

(b) Combination of tuft-images and CFD surface streamlines.

Figure 12. F-16XL-1 three-camera flight tuft data and CFD solution at FC#46 ($\alpha = 10.40^0$; $M_\infty = 0.53$; $R_n = 46.90\times10^6$).

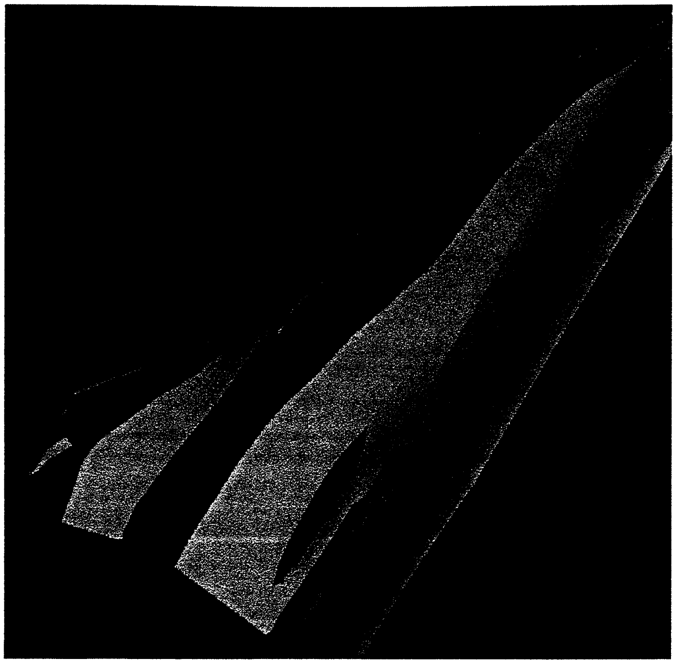

(c) Vortex systems determined from CFD stagnation pressures (PLOT3D) at 0.78.

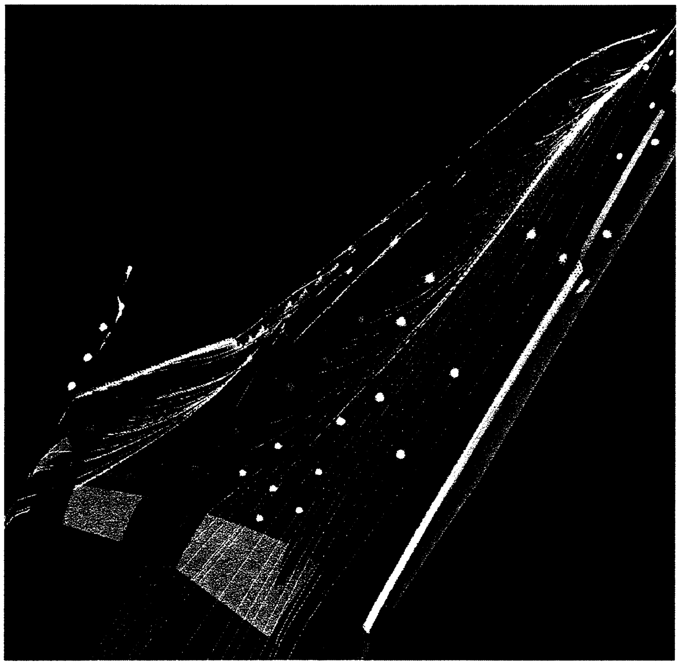

(d) Combination of tuft-images, streamlines, and vortex systems.

Figure 12. Concluded.

At $\alpha = 11.89°$

Upper surface pressures

Figure 13 presents the overall CFD distribution of C_p data at $\alpha = 11.89°$ and $M_\infty = 0.30$ (FC#7 – Flight 145 Run 16B). Unfortunately, the flight C_p data are not recoverable for this flight and therefore no comparison with CFD can be made. An even larger problem is that FC#7 was to be the primary one for doing all surface flow physics comparisons, hence we are missing one large piece. This figure does show some interesting patterns of relative high suction associated with vortices, three inboard and at least two outboard of the crank. The impact of the inboard vortices will become clearer in the following discussion.

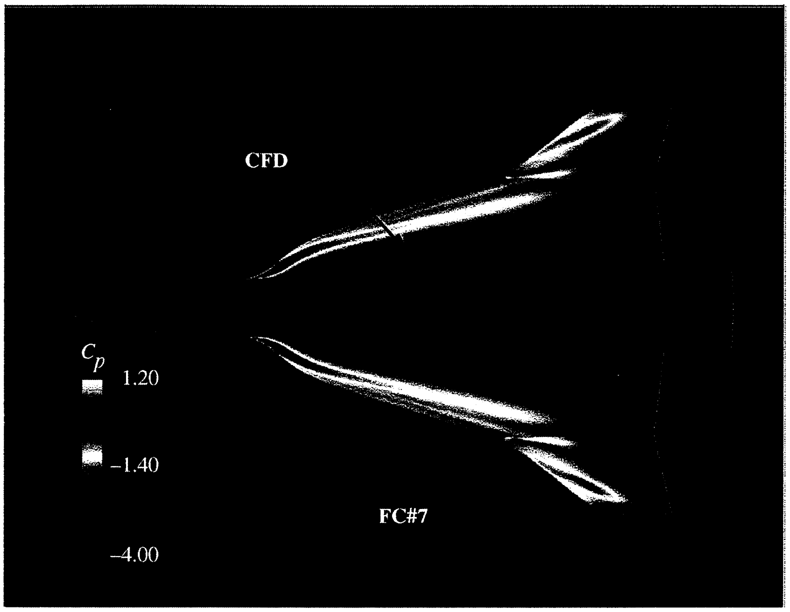

Figure 13. Predicted $C_{p,u}$ distribution of F-16XL-1 at FC#7 ($\alpha = 11.89^0$; $M_\infty = 0.30$; $R_n = 44.4 \times 10^6$).

Boundary Layer Profiles

Figures 14(a), (b), (c), and (d) show the comparison of measured and predicted boundary-layer profiles for rake locations #3, #4, #7, and #5, respectively, at FC#7. These locations were chosen because they had flows which should be markedly different at $\alpha_{nom} = 13°$ and subsonic speeds. At these respective positions, the flows range from (a) being nearly streamwise, (b) underneath the primary vortex, (c) at the secondary separation line, and (d) underneath the secondary vortex. Figure 14(a) also presents an estimate of the profile repeatability for rake #3 because this position was used as a control, flown with each of the others, and had the most benign flow. As can be seen, the experimental velocity ratios only have a small deviation from one another, and the profile is well estimated for $y>0.25$. For $y \leq 0.25$, the measured profile develops more quickly near the surface than predicted, even with the "wall function" option being used in CFL3D.

Underneath the primary vortex (rake #4 location), figure 14(b) shows qualitative agreement between the measured and predicted results but not quantitative. In particular, for $y \leq 0.25$ the predictions are less than measured, and for $y > 0.25$, the reverse is true. Moreover, both results indicate a jet-type flow to commence at $y > 0.3$. Both flows also show regions of quasi-linear variation of velocity with y, indicative of being outside the boundary layer and just into the influence of the primary vortex.

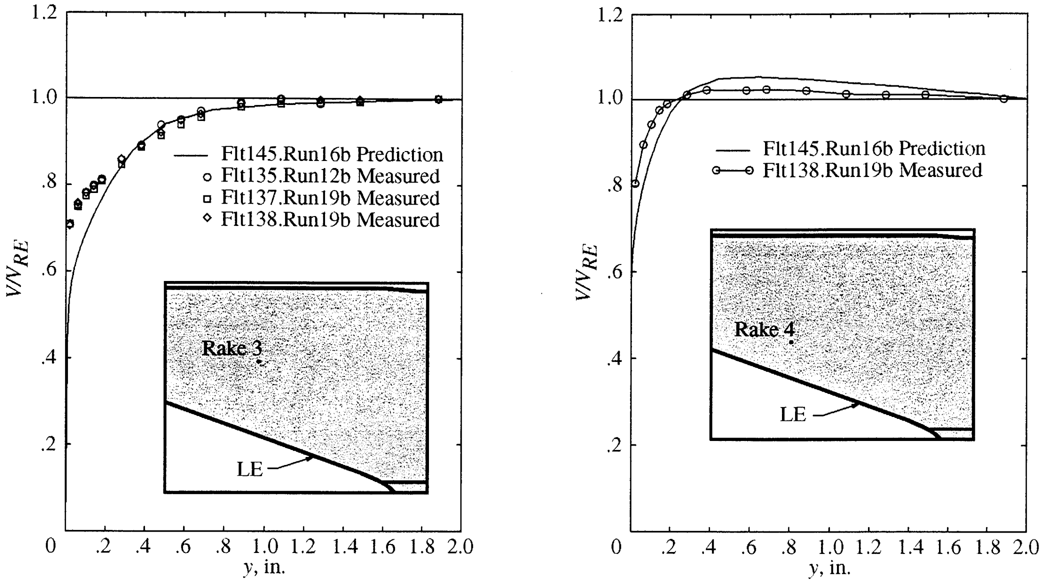

(a) Rake #3

(b) Rake #4.

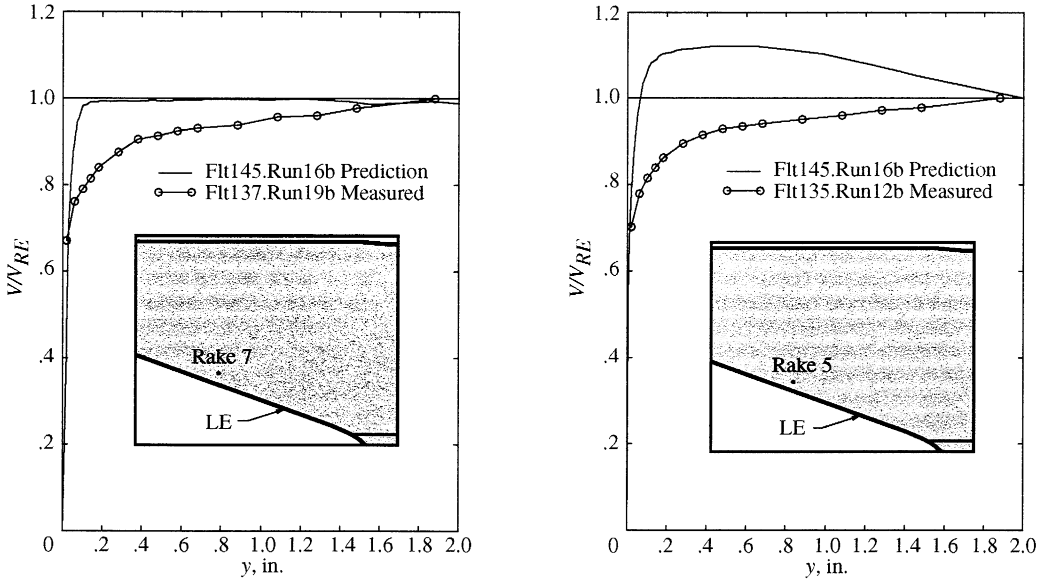

(c) Rake #7.

(d) Rake #5.

Figure 14. Predicted and measured velocity profiles for boundary-layer (B.L.) rakes on F-16XL-1 at $\alpha_{avg} = 11.89^0$; $\beta_{nom} = 0^0$; $M_{\infty,avg} = 0.30$; h = 5000 ft; and $R_n = 44.4\times10^6$.

In the vicinity of the secondary vortex there is general disagreement between the measured and predicted values, as shown in figures 14(c) and 14(d). The predicted values are significantly different, whereas the measured ones look to be similar; moreover, the measured values do not look like what is seen at rake #3 or #4, figures 14(a) or 14(b), respectively. Regarding the EFD/CFD disagreement for rake #7, the predictions indicate that at the originally estimated location of the secondary separation line, the profile develops the edge velocity value only a small distance off the surface and thereafter retains that level. This constancy is in contrast to the measured values which only reach edge velocity near the rake extreme. The measured velocity is not asymptotic at the rake extreme; this leads to the conclusion that the maximum velocity has not been achieved at this location. The measured profile for rake #5, underneath the originally estimated location of the secondary vortex, also only achieves edge velocity near the rake extreme; however, the predicted values are markedly different with jet-type flow velocities occurring near the surface over most of the rake height. Comparing only the EFD profiles for rakes #7 and #5 in figure 15(a) shows the velocity distributions are very similar. Although the plan was to use the results of an initial CFD solution to measure two different boundary-layers profiles associated with two different features of the secondary vortex over this part of the wing, it is apparent that only one was captured. The quasi-linear growth of velocity for y> 0.5 for these profiles is associated with vortices around these boundary-layer rakes because the velocity-field produced outside a representative vortex-system core varies like 1/r.

Even though these predicted boundary-layer profiles were different than those measured, some understanding of the local flow measured closer to the surface may be gained by examining the final CFD solution. Figures 15(b) and (c) have been prepared for that purpose. Figure 15(b) shows the stagnation pressure contours at FS 295 and a representation of these two boundary-layer rakes. From this figure, one can see that the two rakes are computationally located in between the secondary vortex and a third vortex-system, as indicated by the streamwise ribbons, and are not at the planned positions associated with the secondary vortex. (Because the third vortex system is located outboard of the secondary vortex, this system is not called a tertiary vortex. Moreover a tertiary vortex would be under more of the influence of the secondary vortex than it would be of the primary system.) Figure 15(c) locates the origin of the third vortex system as coming from that portion of the flow which crosses the apex in the S-blend curve region and from there proceeds over the primary vortex. Hence, this flow gets swept under the primary and moves outboard where it remains in the vicinity of the wing leading edge, inboard of the crank. This flow interaction accounts for the third vortex sense of rotation. Such a vortex system is unexpected, not seen in experiments, and most likely an artifice of this CFD grid/solution.

Consider again the measured velocity profiles of rakes #7 and #5 in figure 15(a). Based on the close proximity of these two rakes, only a single vortex system outboard of the primary vortex can be confirmed and it is the secondary vortex. Moreover, the actual secondary vortex must be more outboard, and most likely larger, than the predicted one shown in figure 15(c). This flow feature is due to both rakes being encompassed by the actual secondary vortex and the third vortex not really a contributor.

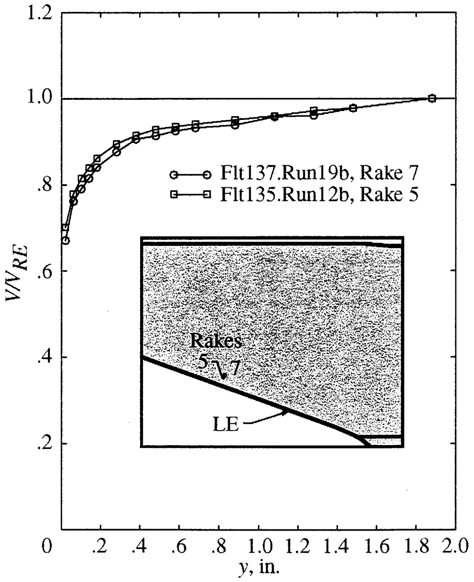

(a) Measured velocity profiles.

Figure 15. Off-surface flow features for boundary-layer rakes #7 and #5 on F-16XL-1 at $\alpha_{avg} = 11.89°$; $\beta_{nom} = 0°$; $M_{\infty,avg} = 0.30$; h = 5000 ft; and $R_n = 44.4 \times 10^6$ and FS 295.

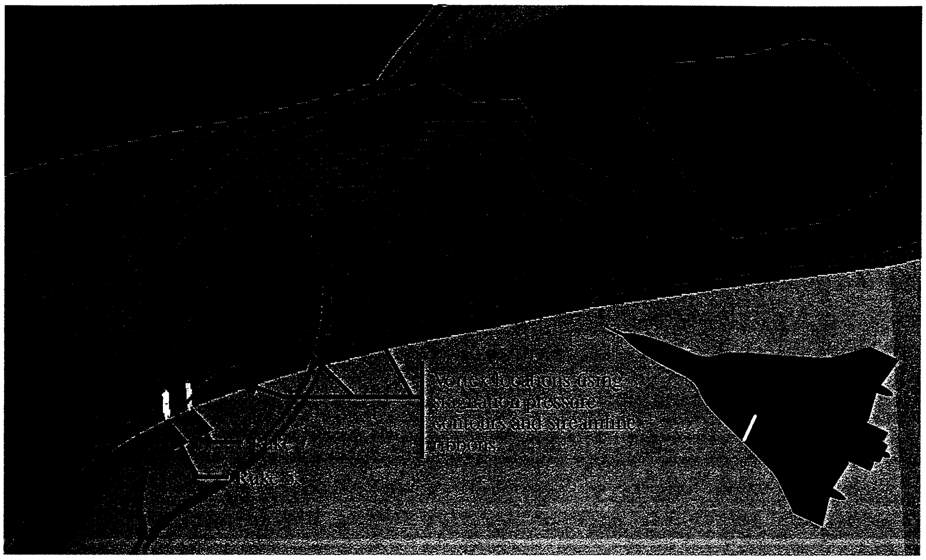

(b) Some predicted vortex systems on inboard wing.

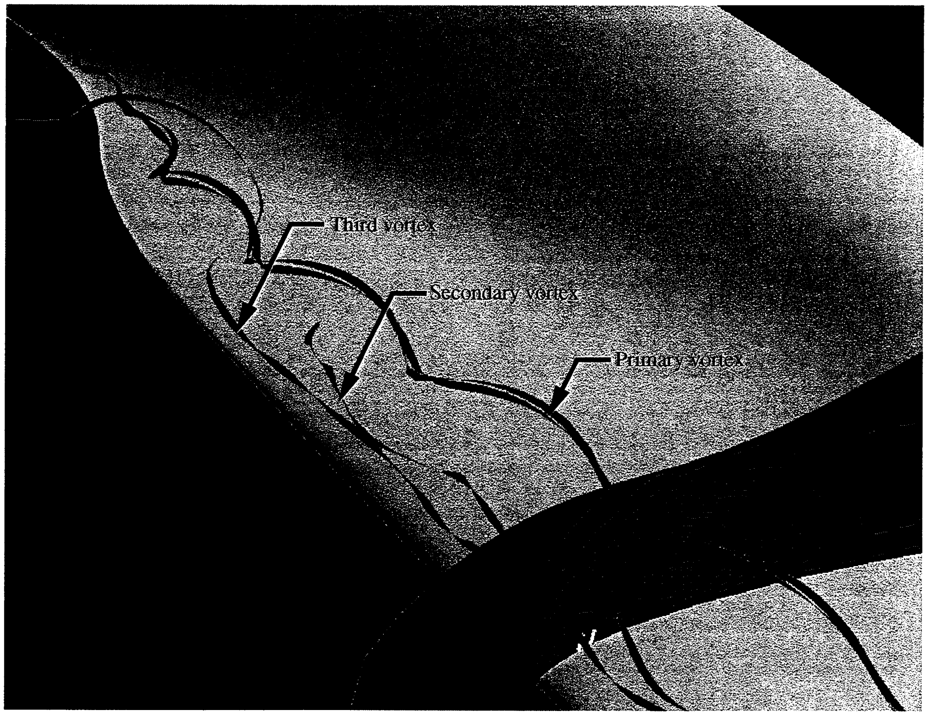

(c) Origination of predicted vortex systems on inboard wing.

Figure 15. Concluded.

Skin friction

Figure 16 provides the measured and predicted c_f values at FS 330 for similar conditions in flight and for CFD. This figure can be used to locate and to assess the impact of the vortex systems because they produce high velocities on the surface which are measured by the modified Preston tubes. Qualitative agreement in shown because both data sets have at least two regions of high c_f, which is indicative of primary and secondary vortices. These vortices occur at BL values near one another; for example, -89 versus -84 for the primary and -108 versus -103 for the secondary, with the measured results given first. The significant differences for the primary vortex are (1) the more restrictive range of BL over which the vortex influence occurs in flight, and (2) the greater levels of c_f reached, that is, measured levels are 39 percent larger than predicted. For the secondary vortex, the measured and predicted levels are comparable but the predicted vortex covers a much narrower range of BL. This result is consistent with the previous discussion of the predicted vortex systems given in figures 15(b) and (c) because the presence of the third vortex is expected to reduce the spanwise extent of the secondary vortex. Moreover, at least two other c_f plateaus or peaks are predicted outboard of the secondary vortex, one at BL -107 and one very near the leading edge at BL -113. The most inboard plateau or peak is more likely to reflect the presence of the predicted third vortex than the one very near the leading-edge because at FS 295 the third vortex is located laterally midway between the secondary vortex and the leading edge (See fig. 15(c)).

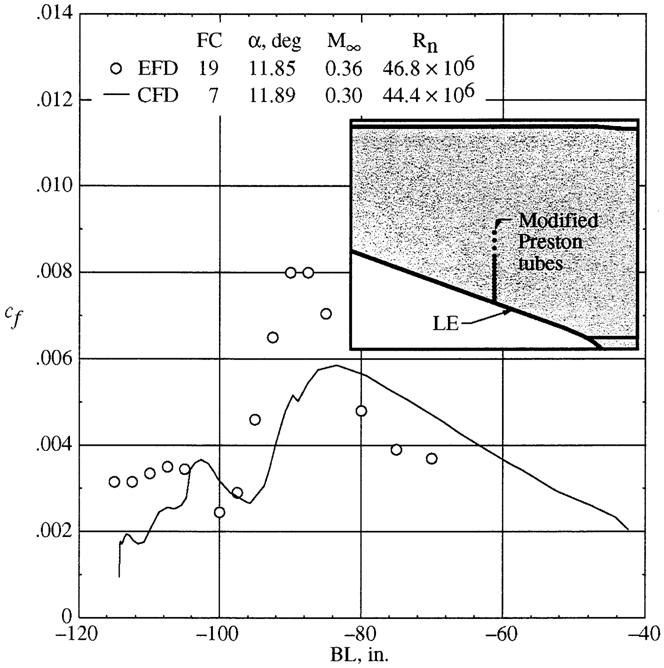

Figure 16. Predicted and measured skin friction coefficient on F-16XL-1at $\alpha_{avg} = 11.87^0$; $\beta_{nom} = 0^0$; M_∞= 0.33; and $R_{n,avg} = 45.6\times10^6$.

Concluding Remarks

- The CFD modeling used has produced reasonably good global C_p comparisons with measured flight data at both transonic and subsonic speeds at the angles of attack presented.
- Regarding the boundary layer comparisons: the profiles were reasonably well predicted inboard and under the primary vortex system. However, the secondary vortex profile was not well predicted either at the anticipated separation point or under the secondary vortex. Moreover, the flight data showed there to be a vortex/boundary-layer interaction to occur in the vicinity of the secondary vortex.
- The spanwise distribution of local skin friction measured data was reasonably well predicted, especially away from the wing leading-edge.
- Lastly, predicted and measured flight-pressures, as well as flight-image data, for the F-16XL-1 airplane are available via the World Wide Web using reference 16.

References

1. Ghaffari, Farhad: *Navier-Stokes, Flight, and Wind Tunnel Flow Analysis for the F/A-18 Aircraft.* NASA TP-3478, December 1994.

2. Potsdam, M.A., Intemann, G.A., Frink, N.T., Campbell, R.L., Smith, L.A.; and Pirzadeh, S.: *Wing/Pylon Fillet Design Using Unstructured Mesh Euler Solvers.* AIAA 93-3500, August 1993.

3. Hillaker, H.J.: F-*16XL Flight Test Program Overview.* AIAA Paper 83-2730, November 1983.

4. Talty, Patrick K.; and Caughlin, Donald J.: *F-16XL Demonstrates New Capabilities in Flight Test at Edwards Air Force Base.* J. Aircraft, Vol.25, No.3, March 1988, pp.206 to 215.

5. Anders, Scott G.; and Fischer, Michael C.: *F-16XL-2 Supersonic Laminar Flow Control Flight Test Experiment.* NASA/TP-1999-209683, December 1999.

6. Lamar, John E., Obara, Clifford J.; Fisher, Bruce D.; and Fisher, David F.: *Flight, Wind-Tunnel and Computational Fluid Dynamics for Cranked Arrow Wing (F-16XL-1) at Subsonic and Transonic Speeds.* NASA/TP-2001-210629, February 2001.

7. Bower, J. N.; and Scott, S. R.: *The F-16XL Flight Test Program.* Soc. of Flight Test Engrs. 15th Ann. Symp. Procs., Aug. 1984, pp. 9-1 to 9-5.

8. Bertelrud, A.: *Total Head/Static Measurements of Skin Friction and Surface Pressure.* AIAA Journal, Vol. 15, No. 3, Mar. 1977, pp. 436–438.

9. Thomas, J. L., Anderson, W. K.; and Krist, S. T.: *Navier-Stokes Computations of Vortical Flows over Low-Aspect-Ratio Wings.* AIAA Journal, Vol. 28, No. 2, Feb. 1990, pp. 205–212.

10. Thomas, J. L.; Weston, R. P.; Luckring, J. M.; Walters, R. W.; Reu, T.; and Ghaffari, F.*: A Patch-Grid Algorithm for Complex Configurations Directed Towards the F-18 Aircraft.* AIAA Paper 89-0121, 1989.

11. White, Frank M.: *Viscous Fluid Flow.* McGraw-Hill Inc., pp. 474-476, 1974.

12. Walatka, Pamela P.; Clucas, Jean; McCabe, R. Kevin; Potter, Rick; and FAST programmers at ARC: *FAST User Guide: Version 1.1a.* RND-3-010, NASA Ames Research Center, Aug. 3, 1999.

13. *Tecplot Version 7.5 User's Manual.* Amtec Engineering, Inc., 1988-1998.

14. *FIELDVIEW Version 6 User's Guide.* Intelligent Light, May 1999.

15. Walatka, Pamela P.; Buning, Pieter G.; Pierce, Larry; and Elson, Patricia A.*: PLOT3D User's Manual.* NASA TM-101067, 1990.

16. Cronin, Catherine K.: *Program for Information Storage and Management---F16XL High Lift Project (CAWAP).* http://CAWAP-prism.larc.nasa.gov/cgi-bin/webprism.cgi?cawap@remote_dbsrv1. Accessed January 4, 2001.